A00-16366

# AIAA 2000–0478

## Simulation of Fuel–Air Mixing and Combustion in a Trapped–Vortex Combustor

Christopher Stone and Suresh Menon
*School of Aerospace Engineering*
*Georgia Institute of Technology*
*Atlanta, Georgia 30332-0150*

**38th AIAA Aerospace Sciences Meeting and Exhibit**
**January 10–13, 2000 / Reno, NV**

# Simulation of Fuel–Air Mixing and Combustion in a Trapped–Vortex Combustor

Christopher Stone* and Suresh Menon†
*School of Aerospace Engineering*
*Georgia Institute of Technology*
*Atlanta, Georgia 30332-0150*

**Fuel/air mixing and combustion in a Trapped–Vortex Combustion (TVC) has been numerically investigated using Large–Eddy Simulation (LES). A previously studied experimental combustor configuration is used to investigate the effects of Reynolds number on fuel/air mixing and combustion properties. It is found that the fuel/air mixing rates are enhanced by a higher annular air velocity for both reacting and non-reacting flow conditions. As a result of the increased mixing rate, the reactions are found to be entirely contained inside the cavity. To further investigate the turbulent mixing properties of the TVC under non-reacting conditions, a new subgrid mixing model for LES using the Linear–Eddy Model (LEM) is developed and applied. Comparison with the conventional gradient-diffusion closure shows that the new closure predicts higher levels of unmixedness in regions dominated by large-scale structures.**

## 1 Introduction

Flame instability is a major cause of reduced combustion efficiencies; evident by increased unburned hydrocarbons ($UHC$). Extreme cases of flame instability can lead to lift-off or even blowout. As a result, many combustion systems are restricted from operating fuel–lean, a desired combustion regime due to its reduced $NO_x$ and post–flame emissions capabilities. A new combustor concept proposed by Hsu *et al.*,[1] uses a vortex trapped inside a cavity to increase flame stability. For this reason, this combustor is referred to as the "Trapped–Vortex" combustor ($TVC$). Various studies into the application of cavity–flow interaction have been conducted in the past; however, most were conducted under non-reacting conditions. The effective vortex locking in a cavity under reacting flow conditions could be quite different. This is due to the volumetric expansion and increased viscosity induced by combustion heat release.

Another potential difficulty was noted by Hsu *et al.*[1] They showed through experiments that a cavity–locked vortex entrains very little main–flow air. This results in a low exchange of mass and heat between the cavity and the main flow. Since combustion requires a continuous supply of reactants, fuel and air must be directly injected in the cavity to sustain the burning processes. However, direct injection (mass addition) can disrupt the flow dynamics, possibly resulting in cavity instability. Previous attempts at numerical modeling of the $TVC$ by Katta *et al.*[2] noted the possibility of mixing–limited reactions in the $TVC$. For this reason, fuel/air mixing and its effect on combustion in the $TVC$ is investigated in this study.

To fully predict combustion characteristics in a practical combustion system such as the $TVC$, the interaction between chemical species and the fluid dynamics must be accurately simulated. In order to have chemical reactions, fuel and air must mix on the molecular level. Several methods exist for modeling or simulating these processes: Direct–Numerical Simulation (DNS), Reynolds–Averaged–Navier–Stokes Simulation (RANS), and Large–Eddy Simulation (LES).

In DNS, all turbulent length scales, from the integral scale $L$, to the Kolmogrov scale $\eta$, are resolved. Therefore, DNS requires no turbulence modeling. For most practical combustion systems with high Reynolds numbers, the range of length scales is extreme, resulting in high grid resolution requirements. The fine resolution requirement of DNS makes it far too expensive for practical combustion modeling. Unlike DNS, RANS attempts to model all the turbulence which allows coarse grid resolution to be used and results in short simulation times. However, since all of the turbulence is modeled, much of the relevant unsteady physics is lost.

As a compromise between DNS and RANS, LES resolves all length scales down to some cut–off size after which the modeling is used. By modeling only the smallest scales of the flow, LES is believed to give a more realistic picture of the governing physics of the flow. Additionally, since the smallest scales are not fully resolved, the resolution requirement is less severe compared to DNS and is, therefore, less expensive in terms of both memory and computational time. As result, LES has the potential to be a practical engineering design tool for problems where unsteady effects are to be resolved.

*Graduate Research Assistant, AIAA Student Member
†Professor, AIAA Senior Member

## 2 Governing Equations

The governing conservation equations of motion for mass, momentum, energy, and species in a compressible, reacting fluid are:

$$\begin{array}{l} \frac{\partial \rho}{\partial t} + \frac{\partial \rho u_i}{\partial x_i} = 0 \\ \frac{\partial \rho u_i}{\partial t} + \frac{\partial}{\partial x_j}[\rho u_i u_j + p\delta_{ij} - \tau_{ij}] = 0 \\ \frac{\partial \rho E}{\partial t} + \frac{\partial}{\partial x_i}[(\rho E + p)u_i + q_i - u_j \tau_{ji}] = 0 \\ \frac{\partial \rho Y_m}{\partial t} + \frac{\partial}{\partial x_i}[\rho Y_m (u_i + V_{i,m})] = \dot{w}_m \quad m = 1, N \end{array} \tag{1}$$

Here, $\rho$ is the mass density, $p$ is the pressure, $E$ is the total energy per unit mass, $u_i$ is the velocity vector, $q_i$ is the heat flux vector, $\tau_{ij}$ is the viscous stress tensor, and $N$ is the total number of chemical species. The individual species mass fraction, diffusion velocities, and mass reaction rate per unit volume are, respectively, $Y_m$, $V_{i,m}$, and $\dot{w}_m$. The viscous stress tensor is $\tau_{ij} = \mu(\partial u_i/\partial x_j + \partial u_j/\partial x_i) - \frac{2}{3}\mu(\partial u_k/\partial x_k)\delta_{ij}$ where $\mu$ is the molecular viscosity coefficient approximated using Sutherland's law. The diffusion velocities are approximated by Fick's law: $V_{i,m} = (-D_m/Y_m)(\partial Y_m/\partial x_i)$ where $D_m$ is the $m$-th species mixture averaged molecular diffusion coefficient. The pressure is determined from the equation of state for a perfect gas mixture

$$P = \rho T \sum_{m=1}^{N} Y_m R_u / W_m \tag{2}$$

where $T$ is the temperature, $R_u$ is the universal gas constant, and $W_m$ the species molecular weight. The total energy per unit volume is determined from $\rho E = \rho(e + \frac{1}{2}u_k^2)$ where $e$ is the internal energy per unit mass given by $e = \sum_{m=1}^{N} Y_m h_m - P/\rho$ and $h_m$ is the species enthalpy. Finally, the caloric equation of state is given by

$$h_m = \Delta h^0_{f,m} + \int_{T^0}^{T} c_{p,m}(T) dT \tag{3}$$

where $\Delta h^0_{f,m}$ is the standard heat of formation at temperature $T^0$ and $c_{p,m}$ is the $m$-th species specific heat at constant pressure.

Following Erlebacher *et al.*,[3] the flow variables can be decomposed into the supergrid (i.e., resolved) and subgrid (i.e., unresolved) components by a spatial filtering operation such that $f = \widetilde{f} + f''$ where $\sim$ and $''$ denote resolved supergrid and unresolved fluctuating subgrid quantities, respectively. The resolved supergrid quantities are determined by Favre filtering:

$$\widetilde{f} = \frac{\overline{\rho f}}{\overline{\rho}} \tag{4}$$

where the overbar represents spatial filtering defined as

$$\overline{f(x_i, t)} = \int f(x_i', t) G_f(x_i, x_i') dx_i'. \tag{5}$$

Here, $G_f$ is the filter kernel and the integral is over the entire domain. Applying the filtering operation (a low-pass filter of grid size $\overline{\Delta}$) to the Navier-Stokes equations, the following LES equations are obtained:

$$\begin{array}{l} \frac{\partial \overline{\rho}}{\partial t} + \frac{\partial \overline{\rho}\widetilde{u}_i}{\partial x_i} = 0 \\ \frac{\partial \overline{\rho}\widetilde{u}_i}{\partial t} + \frac{\partial}{\partial x_j}[\overline{\rho}\widetilde{u}_i\widetilde{u}_j + \overline{p}\,\delta_{ij} - \overline{\tau}_{ij} + \tau_{ij}^{sgs}] = 0 \\ \frac{\partial \overline{\rho}\widetilde{E}}{\partial t} + \frac{\partial}{\partial x_i}[(\overline{\rho}\widetilde{E} + \overline{p})\widetilde{u}_i + \overline{q}_i - \widetilde{u}_j\overline{\tau}_{ji} + H_i^{sgs} + \sigma_{ij}^{sgs}] = 0 \\ \frac{\partial \overline{\rho}\widetilde{Y}_m}{\partial t} + \frac{\partial}{\partial x_i}[\overline{\rho}\widetilde{Y}_m\widetilde{u}_i - \overline{\rho}\bar{D}_m\frac{\partial \widetilde{Y}_m}{\partial x_i} + \Phi_{i,m}^{sgs} + \theta_{i,m}^{sgs}] = \overline{\dot{w}}_m \end{array} \tag{6}$$

Here, $\overline{\tau}_{ij}$ and $\overline{q}_i$ are approximated in terms of the filtered velocity. The unclosed subgrid terms representing respectively, the subgrid stress tensor, subgrid heat flux, unresolved viscous work, species mass flux, diffusive mass flux, and filtered reaction rate are:

$$\begin{array}{rcl} \tau_{ij}^{sgs} & = & \overline{\rho}[\widetilde{u_i u_j} - \widetilde{u}_i\widetilde{u}_j] \\ H_i^{sgs} & = & \overline{\rho}[\widetilde{Eu_i} - \widetilde{E}\widetilde{u}_i] + [\overline{pu_i} - \overline{p}\widetilde{u}_i] \\ \sigma_i^{sgs} & = & [\overline{u_j\tau_{ij}} - \widetilde{u}_j\overline{\tau}_{ij}] \\ \Phi_{i,m}^{sgs} & = & \overline{\rho}[\widetilde{u_i Y_m} - \widetilde{u}_i\widetilde{Y}_m] \\ \theta_{i,m}^{sgs} & = & \overline{\rho}[\widetilde{V_{i,m}Y_m} - \widetilde{V}_{i,m}\widetilde{Y}_m] \\ \overline{\dot{w}}_m. & & \end{array} \tag{7}$$

The closure of several of these terms will now be discussed.

## 3 Subgrid Closure Methodology

The subgrid stress tensor, $\tau_{ij}^{sgs}$, and subgrid heat flux, $H_i^{sgs}$, have been extensively modeled in the past by employing the subgrid kinetic energy equation, $k^{sgs}$, and are, therefore, only briefly discussed. The unresolved viscous work, $\sigma_i^{sgs}$, and the diffusive mass flux, $\theta_{i,m}^{sgs}$, are neglected in this study. Closure of the species mass flux, $\Phi_{i,m}^{sgs}$, is carried out in the present study using a conventional gradient-diffusion model and a new model based on the Linear–Eddy Model (LEM). Closure of the filtered reaction rate term, $\overline{\dot{w}}_m$, is achieved using the conventional Eddy-Break-Up Model (EBU).[6]

### 3.1 Momentum and Energy Transport Closure

In the present approach, the subgrid stress tensor, $\tau_{i,j}^{sgs}$, is determined by using the local grid size, $\overline{\Delta}$, as the characteristic length scale and the subgrid kinetic energy, $k^{sgs}$, as the characteristic velocity scale. The subgrid kinetic energy, $k^{sgs} = \frac{1}{2}[\widetilde{u_k^2} - \widetilde{u}_k^2]$ is obtained by solving the following transport equation:[4]

$$\frac{\partial \overline{\rho}\, k^{sgs}}{\partial t} + \frac{\partial}{\partial x_i}(\overline{\rho}\,\widetilde{u}_i k^{sgs}) = P^{sgs} - D^{sgs} + \frac{\partial}{\partial x_i}\left(\overline{\rho}\,\frac{\nu_t}{Pr_t}\frac{\partial k^{sgs}}{\partial x_i}\right) \tag{8}$$

were $Pr_t$ is the turbulent Prandtl number (taken as constant and equal to 0.90 for this study), $P^{sgs}$ and $D^{sgs}$ are, respectively, the production and dissipation of subgrid kinetic energy. The production term is defined as, $P^{sgs} = -\tau_{ij}^{sgs}(\partial\widetilde{u}_i/\partial x_j)$, where $\tau_{ij}^{sgs}$ is the modeled subgrid stress tensor. $\tau_{ij}^{sgs}$ is modeled as

$$\tau_{ij}^{sgs} = -2\overline{\rho}\,\nu_t(\widetilde{S}_{ij} - \frac{1}{3}\widetilde{S}_{kk}\delta_{ij}) + \frac{2}{3}\overline{\rho}k^{sgs}\delta_{ij} \quad (9)$$

with the eddy viscosity, $\nu_t = C_\nu(k^{sgs})^{1/2}\overline{\Delta}$ where $\overline{\Delta}$ is the characteristic LES grid size and the resolved rate–of–strain tensor, $\widetilde{S}_{ij}, = \frac{1}{2}(\partial\widetilde{u}_i/\partial x_j + \partial\widetilde{u}_j/\partial x_i)$. Finally, the dissipation term is modeled as $D^{sgs} = C_\varepsilon\overline{\rho}(k^{sgs})^{3/2}/\overline{\Delta}$. The coefficients, $C_\nu$ and $C_\varepsilon$ are constants which can be dynamically determined[5] but will be taken as constants and equal to 0.2 and 0.916, respectively. It should be noted that 3-D isotropic turbulent scaling laws were used to derive the preceding relations, and therefore may not be completely applicable in this 2-D study.

The closure of the subgrid heat flux $H_i^{sgs}$ is achieved using a conventional gradient–diffusion model:

$$H_i^{sgs} = -\overline{\rho}\,\frac{\nu_t}{Pr_t}\,\frac{\partial\widetilde{h}}{\partial x_i}, \quad (10)$$

where $\widetilde{h}$ is the resolved scale total mixture enthalpy per unit mass, $\widetilde{h} = \Delta h^0_{f,m} + \int_{T^0}^{T} c_{p,m}(T)dT + \frac{1}{2}u_k^2$.

### 3.2 Subgrid Reaction Rate Closure

Closure of the fluctuating reaction rate, $\overline{\dot{\omega}}_m$, has been accomplished using a conventional *Eddy–Break–Up* model (EBU).[6] Chemical reactions are fundamentally controlled by mixing of the fuel and oxidizer. Therefore, reaction rates are restricted by the scalar mixing rate. In the EBU model, the time scale required for complete molecular mixing is modeled as the time for one subgrid eddy to be completely dissipated (mixed on the molecular level). Since a subgrid eddy can be viewed as having a uniform composition, the time needed to molecularly diffuse the species is the same that needed for complete velocity dissipation. The subgrid fluid dynamic/mixing time scale, $\tau_{mix}$, is proportional to the subgrid turbulent kinetic energy, $k^{sgs}$, and its dissipation rate, $\epsilon^{sgs}$, by the relation:

$$\tau_{mix} \sim \frac{k^{sgs}}{\epsilon^{sgs}} \sim C_{EBU}\frac{\overline{\Delta}}{\sqrt{2k^{sgs}}} \quad (11)$$

Here the scaling constant, $C_{EBU}$, is set to unity following Fureby *et al.*[6] The mixing time-scale reaction rate is then,

$$\dot{\omega}_{mix} = \frac{1}{\tau_{mix}}\,min(\frac{1}{2}[O_2], [CH_4]). \quad (12)$$

The chemical kinetic reaction rate, $\dot{\omega}_{kin}$ is found from the Arrenhius global reaction rate for methane/air combustion. The effective chemical reaction rate, $\dot{\omega}_{ebu}$, is found by taking the minimum of the mixing reaction rate (fluid time scale) and the kinetic rate (chemical time), i.e.;

$$\dot{\omega}_{ebu} = min(\dot{\omega}_{mix}, \dot{\omega}_{kin}). \quad (13)$$

This form of closure effectively treats $\dot{\omega}_{kin}$ as an upper–limit on the overall reaction rate.

### 3.3 Scalar Transport Closure: Gradient-Diffusion

A conventional closure for the subgrid scalar velocity fluctuation term, $\Phi_{i,m}^{sgs}$ is a gradient-diffusion model analogous to that used for $H_i^{sgs}$:

$$\Phi_{i,m}^{sgs} = -\overline{\rho}\,\frac{\nu_t}{Sc_t}\frac{\partial\widetilde{Y}_m}{\partial x_i} \quad (14)$$

where $Sc_t$ is the turbulent Schmidt number found from the product, $Sc_t = Pr_t Le_m$ ($Le_m$ is the species Lewis number). If should be noted that this form of closure effectively treats small scale fluid dynamic effects as molecular processes.

The subgrid diffusive mass flux, $\theta_{i,m}^{sgs}$, is ignored is this study since its contribution is small in comparison to $\Phi_{i,m}^{sgs}$.[7]

### 3.4 Scalar Transport Closure: Linear–Eddy Model

Even though the Linear–Eddy Model (LEM) was first developed as a stand-alone model for scalar mixing in turbulent flows,[8] it has been shown to be an attractive subgrid model for LES simulations.[9–12] An attribute of the LEM is that it separately treats molecular diffusion and turbulent convection, allowing both effects to be realized. Since the LEM is limited to a 1-D domain, a high subgrid resolution is affordable. This high resolution permits all length scales to be fully resolved, avoiding the need for modeling. For this reason, the LEM can be thought of as a subgrid, 1-D DNS.

Previous use of the LEM as a LES subgrid model[13] has simulated the evolution of the scalar field in the subgrid, requiring cell–to–cell scalar transport to model large-scale (supergrid) transport (referred to as "splicing"[14]). This approach, although accurate, is computationally expensive and difficult to implement in complex geometries. In the present study, a simpler approach is developed for engineering studies.

Expanding upon the work of Kim,[7] the scalar fields are carried explicitly in the supergrid (as in conventional LES) while the LEM is used only to determine the subgrid species–velocity correlation, $\Phi_{i,m}^{sgs}$, which is approximated in the subgrid domain as:

$$\Phi_{i,m}^{sgs} \approx \overline{\rho}\widetilde{u_i'Y_m'}. \quad (15)$$

Here, the cross and Leonard type terms are neglected since only the fluctuating term is considered. Since the scalar fields evolve in the supergrid (LES cells), inter-cell convection is not needed. As noted by Kim,[7] this method is more computationally efficient in terms of both CPU time and memory required compared to the splicing technique.

In order to obtain the correlation, $\Phi_{i,m}^{sgs}$, both species and velocity fields must be evolved. In the present LEM subgrid approach, species diffusion and viscous dissipation are treated by solving the 1-D conservation equations. By assuming constant pressure and

without chemical reactions or convection, the diffusion equations are,

$$\frac{\partial Y_m}{\partial t} = -\frac{1}{\rho}\frac{\partial \rho Y_m V_m}{\partial s} + F_m^{stir} \tag{16}$$

$$\frac{\partial u}{\partial t} = \nu\frac{\partial^2 u}{\partial s^2} + F_u^{stir}, \tag{17}$$

where $s$ is the subgrid domain of size $\overline{\Delta}$. As with the resolved scale, $V_m$, is assumed to be Fickian. Eqs. 16 & 17 are marched forward in time by employing a second order–accurate, backward Euler time integration scheme. The resulting explicit time–step for the subgrid molecular transport is

$$\Delta t_{diff} = C_{diff}\frac{\overline{\Delta}}{\max(\nu, D_m)}, \tag{18}$$

where $C_{diff}$ is a numerical stability constant set to 0.25.

Since turbulent convection is implemented explicitly, the convective terms $u\frac{\partial Y_m}{\partial x}$ and $u\frac{\partial u}{\partial x}$ are symbolically represented in Eqs. 16 & 17 as $F_m^{stir}$ and $F_u^{stir}$, respectively. Turbulent stirring within the domain $\eta \le s \le \overline{\Delta}$, is modeled stochastically as a set of instantaneous rearrangements of the 1-D scalar fields. Each rearrangement mimics the action of a single eddy (of size smaller than $\overline{\Delta}$) on the scalar field. The frequency and the size of the rearrangements is determined from 3-D inertial–range scaling laws.[15]

The size of the subgrid eddys are randomly determined from a PDF of eddy sizes,

$$f(l) = \frac{5}{3}\frac{l^{-8/3}}{\eta^{-5/3} - \overline{\Delta}^{-5/3}} \tag{19}$$

in the range $\eta < l < \overline{\Delta}$. The Kolmogrov scale, $\eta$, is determined from the turbulent length scale relation

$$\frac{\eta}{\overline{\Delta}} = N_\eta Re^{-3/4}, \tag{20}$$

where $N_\eta$ is a scaling parameter set to unity and $Re = \sqrt{\frac{2}{3}k^{sgs}}\overline{\Delta}/\nu$ (the subgrid turbulent Reynolds number).

In the LEM, the rearrangement (event) rate is determined by first relating fluid element diffusivity to the random walk of a marker particle and then by determining the total turbulent diffusion of that marker particle induced by the action of turbulent eddys (of size ranging from $\overline{\Delta}$ to $\eta$). This is expressed as,

$$D_t \approx \nu(\overline{\Delta}/\eta)^{4/3} = \frac{2}{27}\lambda\int_\eta^{\overline{\Delta}} l^3 f(l)\,dl, \tag{21}$$

where $\lambda$, is the event frequency per unit length and is is determined as:

$$\lambda = \frac{54}{5}\frac{\nu Re}{\overline{\Delta}^3}\frac{[(\overline{\Delta}/\eta)^{5/3} - 1]}{[1 - (\eta/\overline{\Delta})^{4/3}]}. \tag{22}$$

Finally, the resulting stirring time-step is,

$$\Delta t_{stir} = 1/\lambda\overline{\Delta}. \tag{23}$$

The scalar rearrangements are implemented through a process referred to as "triplet mapping".[16] The mapping process generates three copies of the initial scalar field on which the eddy acts in the following manner: (1) all three copies are compressed by a factor of three, (2) the middle segment is reversed, (3) and finally, the new field is formed by super–imposing the three segments. As a result of the triplet nature of the mapping process, each rearrangement requires at least six LEM cells; thereby, requiring $\eta$ to be resolved by six cells.

In the present study, the subgrid fields are reinitialized at every time level. Therefore, initial profiles for the fluctuating species concentration field, $Y_m''$, and the fluctuating velocity field, $u_i''$, must be given. Assuming the subgrid fields are isotropic, the fluctuating velocity $u_i''$, can be approximated as the subgrid turbulent intensity, $\sqrt{\frac{2}{3}k^{sgs}}$. The $u''$ profile has a magnitude ranging from $\pm\sqrt{\frac{2}{3}k^{sgs}}$ taken about a zero mean. An example of the LEM velocity initialization is shown in Fig. 1(a). There, one up–down segment represents a single eddy of size $\eta$. The number of initial eddys was calculated as the integer ratio of the LEM domain size and the initial eddy size, i.e., $N_{eddys} \approx \overline{\Delta}/\eta$.

The initial $Y_m''$ profile corresponding to $u''$ is shown in Fig. 1(b). As can be seen, the characteristic eddy size is twice that of $u''$. Physically, this corresponds to a single eddy having a uniform concentration. The $Y_m''$ fluctuations are taken about the resolved mean concentration, $\tilde{Y}_m$ so as to keep the local ensemble average equal to $\tilde{Y}_m$.

Since the subgrid LEM is reinitialized at every LES time level, some initial, non-physical time evolution must be used to allow the LEM fields to evolve to a physically significant state. For this study, the LEM evolution time was set equal to the global convective time scale, $\Delta t_{conv}$[1] ( $> \Delta t_{LES}$). Therefore, at every LES time level, the LEM fields are reinitialized, evolved over an entire $\Delta t_{conv}$. Finally, $\Phi_{i,m}^{sgs}$ is determined by first directly computing the velocity-species correlation over the entire LEM domain and then ensemble-averaging this correlation in each LEM domain.

## 4 Numerical Modeling

The numerical algorithm used here solves the fully compressible, unsteady Navier-Stokes equations along with the species conservation and the turbulent kinetic energy by a finite-volume method which is second-order accurate in both space and time. The equa-

[1]The convective time step, $\Delta t_{conv} \approx \overline{\Delta}/u_{max}$, is separately computed and is not the time step of the compressible algorithm, $\Delta t_{LES}$, which is controlled by the acoustic time–scale.

**Table 1 Single-processor hours per flow-through time on a Cray-T3E (Stennis Space Center, NAVO) and SGI-Origin 2000 (Wright-Paterson AFB, ASC) for 2-D LES algorithm. Grid is 580 x 138.**

| Platform | Mixing/ LES | Mixing/ LES-LEM | Finite Reaction |
|---|---|---|---|
| SGI-Origin 2000 | — | — | 120 |
| Cray-T3E | 90 | 635 | 240 |

tions are solved by time–marching the governing conservation equations with the MacCormack Predictor–Corrector time–stepping scheme. Standard no–slip, adiabatic wall conditions conditions are used with characteristic inflow/outflow boundary conditions following the work of Baum *et al.*[17] and Poinsot *et al.*[18]

The $TVC$ modeling configuration, (shown in Fig. 2), is the same used by Katta *et al.*[19] The $TVC$ geometry consists of a $70mm$ diameter flat cylindrical fore-body surrounded by a cylinder of $80mm$ (inner diameter). A 20 x $50.8mm$ cylindrical after-body is placed $30mm$ downstream of the fore-body. A $9mm$ cylinder is used to connect the fore- and after-bodies. $1mm$ fuel and air jets are located 19, 14, and $11mm$ (radially) from the centerline on the cavity side of the after-body to allow direct injection into the cavity. The jet velocities are 12.4, 11.5, 12.4 m/s respectively with fuel (methane) injected from the center jet and air from the two outer jets. The primary equivalence ratio ($\phi_{jets}$), defined as fuel–to–air ratio of injected mass versus that of stoichiometric, is 4.4. Two inlet air velocities, 20 and 40 m/s, are used resulting in Reynolds numbers of approximately 6,250 and 12,500, based on the inlet duct height of $5mm$. A highly resolved computational grid of 580 x 138 ($\Delta$x and $\Delta$y $\sim$ 0.25mm in the shear–layer and cavity regions) is employed with clustering at the walls and corners. Parabolic velocity profiles are used for the inlet and fuel/air injection ports.

A single step, global chemical mechanism for methane/air combustion (Eqn. 24) is employed with a molar reaction rate in Arrenhius form.

$$CH_4 + 2O_2 + 7.52N_2 \Rightarrow CO_2 + 2H_2O + 7.52N_2. \quad (24)$$

A pre–exponential term $A = 8.3 * 10^5$(gmol/cm) and an activation energy, $E_a$ = 7,500 (kcal/gmol) are used.

The numerical algorithm is implemented in parallel using Message-Passing-Interface (MPI) and is highly optimized. Typical simulation costs (Single-processor hours per flow-through time, were a flow-through time is the time needed for a fluid element to traverse the combustor) are tabulated in Table [1] for the Cray-T3E (Stennis Space Center, NAVO) and SGI-Origin 2000 (Wright-Patterson AFB, ASC).

**Table 2 Test conditions used for Trapped–Vortex Combustor numerical simulations.**

| Case | Closure $\Phi_{i,m}^{sgs}$ | Flow Condition | Inflow $U_o$ (m/s) | $t_o$ |
|---|---|---|---|---|
| I | Grad–Diff | Non-React | 20.0 | 7.11 |
| II | Grad–Diff | Non-React | 40.0 | 9.12 |
| III | LEM | Non-React | 40.0 | 7.68 |
| IV | Grad–Diff | React | 20.0 | 7.20 |
| V | Grad–Diff | React | 40.0 | 7.63 |

## 5 Results and Discussion

To investigate the fuel/air mixing properties of the TVC, both reacting and non–reacting simulations were conducted. The five simulations conducted are tabulated in Table [2] with the flow conditions and closure method listed. The terms given in Table [2] are defined as, $\Phi_{i,m}^{sgs}$: subgrid closure method, Condition: reacting flow or non–reacting flow, $U_o$(m/s): annular air inflow velocity, $t_o$: non-dimensional simulation time over which averaging was done (typically, averaging is begun after 5-6 flow-through times to wash out the initial transients). Three non-reacting simulations (I, II, & III) were conducted to investigate the fluid dynamic mixing properties of the TVC and to evaluate the LEM subgrid closure model. The two reacting simulations (IV & V) were conducted in order to investigate the effects of combustion on fuel/air mixing and annular/cavity flow interaction.

### 5.1 Inflow Velocity Effects on Non–Reacting Mixing

To investigate the fluid dynamic mixing properties of the $TVC$, two cases (I & II) were conducted under non-reacting flow conditions. Of key importance in the fuel/air mixing in the $TVC$ is the ability of the annular air to mix with the cavity–injected fuel. Since the amount of fuel injected is far above stoichiometric ($\phi = 4.4$), annular air must be entrained into the cavity in order for the fuel to be completely consumed.

To increase mixing rates, higher turbulence levels are desired. For qualitative analysis, the time averaged mean velocity, $< \widetilde{u}_i >$, and the RMS velocity, $\widetilde{u}_i^{RMS}$, have been computed. Regions of high mean and, perhaps more importantly, high RMS velocities will tend to enhance mixing rates. Figures 3 & 4 show the time averaged mean and RMS velocity profiles for cases I & II. For the higher annular inflow velocity (case II, $U_o$ = 40 m/s), the inner cavity velocity is much higher at all three axial locations compared to case I. One interesting observation is that the RMS velocities are not greatly affected by the higher velocity while the mean velocities increased nearly three-fold. In the near wall region of the dump plane (near the fore-body step), the mean and RMS velocities are higher for case II. This region is of critical importance since vortex shedding initiates from the step. These large scale structures

aid in the fuel/air mixing and combustion in the outer edges of the $TVC$.

For enhanced visualization, the time averaged and instantaneous velocity vectors for cases I & II are shown in Figs. 5(a) & 5(b). The higher annular flow rate (Fig. 5(b)) enhances the trapped-vortex strength, allowing for increased annular/cavity flow interaction. In the time averaged results, it is seen that two vortices are present for case I. In addition to a vortex rotating in the direction of the annular flow, the second vortex rotates in the reverse direction. However, these paired vortices are not present in case II. Rather, only a single, large vortex rotates with the flow.

Mixing with annular air inside the cavity must precede combustion since the injected fuel/air equivalence ratio is great than unity. The mixing rate is enhanced by the increased annular velocity. This is evident by observing the mean fuel concentration levels for cases I & II. The mean and RMS fuel mass fraction radial profiles for both cases have been plotted in Figs. 6 & 7. Near the injection ports, the injected fuel is more quickly dissipated into the surrounding air (Figs. 6(a) & 7(a)) (axial location is $5mm$ away from the ports). Near the fore-body wall (x = $35mm$) the fuel concentrations are nearly uniform up to the step (r = $35mm$) for both cases. However, the actual mass fraction is nearly half for case II. If converted to mixture fraction space, $Z$, the local concentration is nearly at the stoichiometric ratio ($Z = Z_{st}$) of 0.055 for case II. This trend is the same for all three axial locations. In addition to the mean fuel concentration, the RMS fluctuations are affected (unlike the velocities). As with the mean mass fraction, the RMS fluctuating level is reduced by 1/2 for the higher annular velocity. The lower RMS signifies an increased species uniformity achieved with the higher velocity due to the reduction in mixing time.

### 5.2 Inflow Velocity Effects on Reacting Flows

Two reacting-flow cases (IV & V) were used to investigate the impact of fuel/air mixing rates under reacting conditions. The primary equivalence ratio of the cavity jets in both cases was 4.4 and the injection temperature was a slightly elevated value of $500K$. As observed by Sturgess *et al.*,[20] the cavity flow entrains relatively little annulus air and will tend to be fuel–rich under reacting flow conditions. To investigate this, the mean fuel and oxygen mass fractions were studied. Shown in Figs. 8 & 9, are the time averaged mass fractions, $< \widetilde{Y}_m >$, and the RMS concentration, $\widetilde{Y}_m^{RMS}$, of methane and oxygen. Near the injection ports, the RMS values are much higher due to fluctuations in velocity and species composition. Far from the injectors, however (near the fore-body wall), the oxygen is almost entirely consumed leaving a fuel–rich cavity region, although the mean fuel concentration is still high. The remaining fuel is finally consumed outside the cavity in either the dump shear layer or downstream of the after-body, depending on the inlet flow velocity.

Away from the injection ports, the oxygen mean and RMS concentrations are low while the fuel mean and RMS concentration are still large. Since there is too little oxygen to sustain the reaction, the concentration fluctuations must be induced purely by fluid dynamics. Similar trends should be present in other scalar profiles, such as temperature. Figs. 10 & 11 show the corresponding temperature profiles for cases IV & V at the same axial locations. The same scalar mixing effect is observed away from the injection ports signifying that the fluctuations are induced by the fluid dynamics, not by the reaction, i.e., the cavity reaction is localized near the injection ports.

By comparing the concentration profiles of the cases IV and V, it is seen that more fuel is consumed in the cavity for higher inflow velocities. This is evident in the dump shear layer[2]. In Fig. 12, the fuel concentration has been spatially averaged over the dump shear layer. It is seen that the higher velocity case shows a faster drop in $< \widetilde{Y}_{CH_4} >$, signifying that the fuel is consumed more completely inside the cavity.

An alternative method for quantifying the rate at which the fuel is mixed is by examining the species mixture fraction, $Z$, as a function of inflow velocity. Shown in Figs. 13(a) and 13(b) are the instantaneous and time averaged stoichiometric mixture fraction surfaces, $Z = Z_{st}$, for both reacting flow cases (The stoichiometric surface, $Z_{st}$, has been highlighted by a single black line, where $Z_{st}$ for methane air is approximately 0.055). As can be seen in Fig. 13(b) ($U_o = 40$ m/s), $Z_{st}$ is almost entirely contained inside the cavity region for both the instantaneous and the time averaged results. For the lower inflow velocity, the surface extends far downstream of the cavity zone.

Figures 13(a) and 13(b) also show the instantaneous and time-averaged temperature color contours for cases IV & V . Following the same trends are $Z$, the peak temperature regions are seen to shift from outside the cavity region for a lower annular velocity to inside the cavity in case V. In both mean and instantaneous views, the cavity temperature increases with increased flow velocity. Comparison with experimental data is possible for case V. The mean and RMS temperature profiles reported by Hsu *et al.*[1] (obtained with the $CARS$ technique) are super-imposed in Fig. 11. The combustor conditions were nearly identical to those simulated in case V, $U_o = 42$ m/s, $\phi = 4.4$, H/d = 0.59; however, propane instead of methane was used as the primary fuel. Despite this difference, the mean temperature trends should still be comparable. A maximum instantaneous temperature of 2025 K was obtained inside the cavity in case II which is slightly

[2]The dump shear layer is defined as $25.4mm \leq r \leq 35mm$ and $30mm \leq x \leq 90mm$.

lower then the 2150 K reported by Hsu *et al.*[1]

For both inflow velocities, the mean temperature near the injection ports has not been greatly affected. However, away from the injectors, the higher inflow velocity resulted in higher cavity temperatures for both mean and instantaneous profiles. The highest RMS temperature region for both inflow velocities is near the injection ports. An important observation is that the peak temperature region for the case IV was not inside the cavity but downstream in the after-body wake resulting in longer thermal residence times. The longer residence times may increase thermal $NO_x$ production. As would be expected with the higher inflow velocity, the downstream temperature is lower despite higher cavity temperatures. This mainly due to the higher volume flow rate and lower overall equivalence ratio. The combination of a higher fuel consumption rate and higher velocity results in a lower thermal residence time. This is beneficial to lower combustion pollutant formation.

### 5.3 Analyses of the Subgrid Closure

To investigate the properties of the new LEM closure, two test cases (II & III) were conducted under non-reacting conditions. As previously mentioned, the new LEM closure model avoids the gradient diffusion assumption of the conventional closure technique. Counter–gradient diffusion is usually associated with large–scale structures, such as those found in separated shear layers. It should be noted that in LES, the closure of $\Phi_{i,m}^{sgs}$ is at the subgrid level. Therefore, regardless of the choice of this closure for $\Phi_{i,m}^{sgs}$, (gradient diffusion or LEM) the resolved scale time-averaged profiles (as in RANS) are not constrained since counter-gradient diffusion (if it exists) at the large (resolved) scales is automatically captured. This is an advantage of LES that RANS lacks.

The above ability is demonstrated in Fig. 14 where the LES resolved velocity, $\widetilde{u}_i$ and species, $\widetilde{Y}_m$, fields from case II are used to compute the time-averaged correlation as in RANS:

$$-\widetilde{<u_i''Y_m''>} = <\widetilde{u}_i><\widetilde{Y}_m> - <\widetilde{u}_i\widetilde{Y}_m> . \quad (25)$$

In Fig. 14, the term, $-\widetilde{<v''Y''>}$ is compared against the mean scalar radial gradient, $\frac{\partial <\widetilde{Y}>}{\partial y}$ (the species is methane in both profiles). In regions were the scalar gradient and the turbulent closure term positively correlated, gradient-diffusion assumption is valid; however, it is invalid in regions of negative correlation. Two dominant regions of negative correlation are evident in Fig. 14, one in the shear-layer just behind the first step ($x \simeq 35mm$) and the other in the lower regions of the cavity ($x \simeq 50mm$). As seen in Fig. 5(b), the cavity region is dominated by large-scale, coherent structures. In the dump shear layer, the large–scale structures are mostly shed vortices from the cavity lip. Inside the cavity, both the spatially locked, roughly stationary vortex and smaller scale structures formed by the primary injectors combine to give significant counter–gradient diffusion regions.

The ratio of the magnitudes of the LEM and gradient-diffusion closure for $\widetilde{u_i''Y_m''}$ is defined as $\sigma$:

$$\sigma = \frac{-\overline{\rho}\frac{\nu_t}{Sc_t}\frac{\partial \widetilde{Y}_m}{\partial x_i}}{|-\overline{\rho}\widetilde{u_i''Y_m''}|_{LEM}} \quad (26)$$

To find $\sigma$, the magnitudes of the modeled closure term, Eqn. 14, and the LEM closure method, Eqn. 15, were directly compared as a function of subgrid Reynolds number, $Re^{sgs}$. It was found that the LEM closure is similar to the gradient–diffusion closure as $Re^{sgs}$ increases. Figure 15 shows $\sigma$ taken over the entire cavity and shear–layer region from cases II & III. The ratio is seen to increase as a function of the subgrid Reynolds number although in general, it remains on the order of unity. In regions of low $\mathrm{Re}^{sgs}$, the ratio is far from unity (nearing infinity since the turbulent kinetic energy, $k^{sgs}$, rapidly approaches zero) indicating a lower limit for the LEM closure. However, in general, it appears that in regions of high $\mathrm{Re}^{sgs}$ both models have similar magnitudes (but not necessarily the same sign).

Shown in Fig. 16, are the time averaged methane mass fractions at 35 and $50mm$ (axial) from the conventional (case II) and LEM (case III) simulations. The LEM closure yields higher mean and RMS fuel mass fractions inside the cavity region. This is consistent with the results of Kim,[7] in which higher levels of unmixedness were observed when using the LEM closure methodology. The most pronounced differences are at $x = 50mm$. As reported in the time-averaged, RANS level results (Fig. 14), this region is mostly dominated by counter–gradient diffusion and should therefore, be expected to show the greatest differences. A similar trend is seen at $x = 35mm$, where the main vortex roll–up occurs.

## 6 Conclusions

Fuel/air mixing under reacting and non–reacting flow conditions is simulated in a Trapped–Vortex Combustor. The effects of annular inflow velocity on the fluid dynamic mixing properties in the $TVC$ is studied under non-reacting flow conditions. It is found that an higher annular velocity increases the fuel/air mixing rate two-fold (approximately). The higher inflow velocity increases the spatially locked vortex strength and increases the overall mixing in the cavity by reducing the characteristic mixing time.

The effects of annular flow on the reaction characteristics is also investigated. It is found that for a fuel-rich primary jet equivalence ratio of 4.4, the location of the reaction surface is a function of annular air flow rate. For an inflow velocity of 40 m/s, reactions are almost entirely contained inside the cavity,

resulting in higher cavity temperatures and fuel consumption rates. Two reaction zones are identified as (1) a region near the primary fuel/air injection ports where the injected oxygen is initially consumed and (2) along the dump plane were the rest of fuel is finally consumed. It is concluded that the higher annular flow rate increases both the fuel/air mixing rate along the dump plane and the inner cavity region, resulting in a more contained reaction.

To further investigate the impact of scalar-velocity subgrid closure on fuel-air mixing, a conventional gradient-diffusion and a new LEM-based closure for $\Phi_{i,m}^{sgs}$ are compared. The new methodology separately treats molecular diffusion and turbulent stirring and simulates the evolution of the scalar-velocity correlation, thereby avoiding the gradient–diffusion assumption of the conventional closure. Time-averaged (RANS-level) results reveal regions inside the combustor cavity which are dominated by counter–gradient diffusion. When applied, the LEM closure technique results in a lower fuel/air mixing rate and higher fuel mass fraction concentration inside the cavity region. This effect is most significant in regions dominated by large scale structures (i.e. the dump plane and the middle cavity region) which are more conducive to counter–gradient diffusion. How this impacts combustion and heat release remains to be evaluated. This study is underway and will be reported in the near future.

## 7 Acknowledgments

Computational support for this study was provided under the DOD HPC Grand Challenge Project. MSRC computer resources used include ASC, Wright-Patterson AFB and NAVO, Stennis Space Center.

## References

[1] Hsu, K.-Y., Goss, L. P., and Roquemore, W. M., "Characteristics of a Trapped–Vortex Combustor," *Journal of Propulsion and Power*, Vol. 14, No. 1, 1998, pp. 1–12.

[2] Katta, V. and Roquemore, W., "Numerical studies on trapped–vortex combustor," *AIAA-96-2660*, 1996.

[3] Erlebacher, G., Hussaini, M. Y., Speziale, C. G., and Zang, T. A., "Toward the Large-Eddy Simulation of Compressible Turbulent Flows," *Journal of Fluid Mechanics*, Vol. 238, 1992, pp. 155–185.

[4] Menon, S., Yeung, P.-K., and Kim, W.-W., "Effect of Subgrid Models on the Computed Interscale Energy Transfer in Isotropic Turbulence," *Computers and Fluids*, Vol. 25, No. 2, 1996, pp. 165–180.

[5] Kim, W.-W., *A New Dynamic Subgrid-Scale Model for Large-Eddy Simulation of Turbulent Flows*, Ph.D. thesis, Georgia Institute of Technology, Atlanta, GA, September 1996.

[6] Fureby, C. and Lofstrom, C., "Large-Eddy Simulations of bluff body stabilized flames," *Twenty-Fifth Symposium (International) on Combustion*, 1994, pp. 1257–1264.

[7] Kim, W.-W. and Menon, S., "Numerical modeling for fuel/air mixing in a dry low–emission premixer," *Second AFOSR International Conference on DNS and LES*, 1999.

[8] Kerstein, A. R., "Linear-Eddy Model of turbulent Scalar Transport and Mixing," *Combustion Science and Technology*, Vol. 60, 1988, pp. 391–421.

[9] Calhoon, W. H. and Menon, S., "Linear-Eddy Subgrid Model for Reacting Large-Eddy Simulations: Heat Release Effects," *AIAA-97-0368*, 1997.

[10] Menon, S., McMurtry, P., and Kerstein, A. R., "A Linear Eddy Mixing Model for Large Eddy Simulation of Turbulent Combustion," *LES of Complex Engineering and Geophysical Flows*, edited by B. Galperin and S. Orszag, Cambridge University Press, 1993.

[11] Smith, T. M. and Menon, S., "Subgrid Combustion Modeling for Premixed Turbulent Reacting Flows," *AIAA-98-0242*, 1998.

[12] Chakravarthy, V. K. and Menon, S., "Large eddy simulations of stationary premixed flames using a subgrid flamelet approach," *Second AFOSR International Conference on DNS and LES*, 1999.

[13] Chakravarthy, V. K. and Menon, S., "Modeling of turbulent premixed flames in the flamet regime," *First Symposium on Turbulence and Shear Flow Phenomena*, 1999.

[14] Smith, T. M., *Unsteady Simulations of Turbulent Premixed Reacting Flows*, Ph.D. thesis, Georgia Institute of Technology, Atlanta, GA, March 1998.

[15] Kerstein, A. R., "Linear-Eddy Modeling of Turbulent Transport. Part 4. Structure of Diffusion-Flames," *Combustion Science and Technology*, Vol. 81, 1992, pp. 75–86.

[16] Kerstein, A. R., "Linear-Eddy Modeling of Turbulent Transport. Part V: Geometry of Scalar Interfaces," *Physics of Fluids A*, Vol. 3, No. 5, 1991, pp. 1110–1114.

[17] Baum, M., Poinsot, T., and Thevenin, D., "Accurate boundary conditions for multicomponent reactive flows," *Journal of Computational Physics*, Vol. 116, 1994, pp. 247–261.

[18] Poinsot, T. and Lele, S., "Boundary Conditions for Direct Simulations of Compressible Viscous Flow," *Journal of Computational Physics*, Vol. 101, 1992, pp. 104–129.

[19] Katta, V. and Roquemore, W., "Simulation of Unsteady Flows in a Axisymmetric Research Combustor Using Detailed–Chemical Kinetics," *AIAA 98-3766*, 1998.

[20] Sturgess, G. and Hsu, K.-Y., "Entrainment of mainstream flow in a trapped–vortex combustor," *AIAA-97-0261*, 1997.

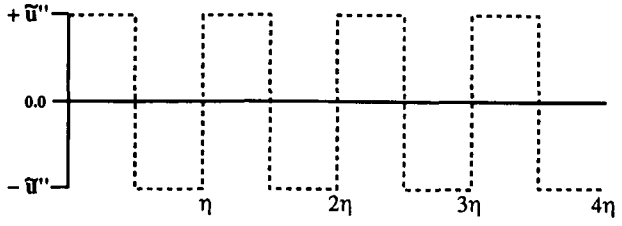


**a)** LEM subgrid velocity field initialization. One (+/-) structure represents one subgrid eddy of size $\eta$. Fluctuating velocity magnitude = $\pm\sqrt{k^{sgs}}$.

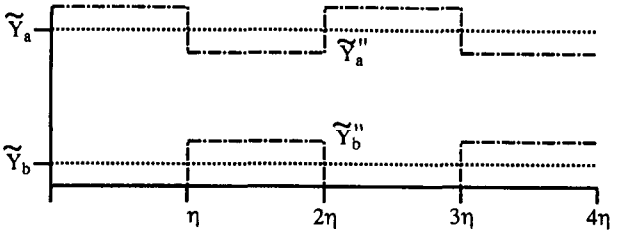


**b)** LEM subgrid scalar field initialization. Each subgrid eddy is given a uniform scalar field. $\widetilde{Y}_m''$ fluctuates about resolved scale (supergrid) scalar value, $\widetilde{Y}_m$. $\widetilde{Y}_a'' = \pm(1 - \widetilde{Y}_a)$ were $\widetilde{Y}_a$ = max($\widetilde{Y}_m$), $\widetilde{Y}_b'' = (1 - \widetilde{Y}_a'')$.

**Fig. 1 LEM fluctuating field initialization.**

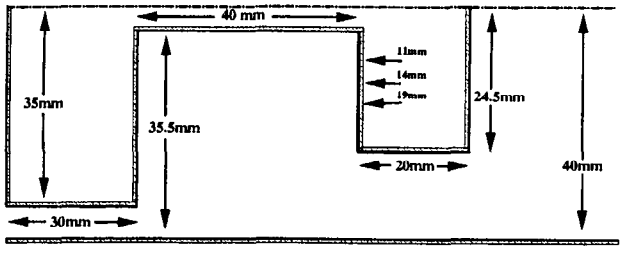


**Fig. 2 Trapped–Vortex geometry used in this numerical study. Total length (x) = 285$mm$.**

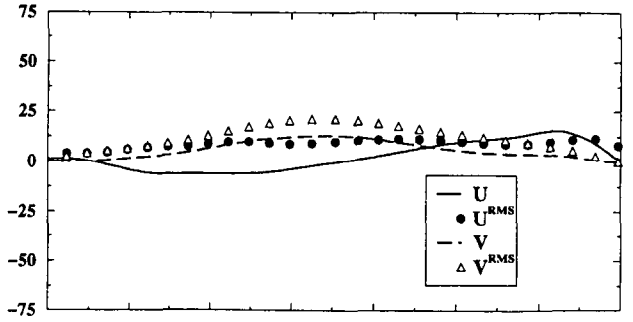


**a)** $x = 65mm$

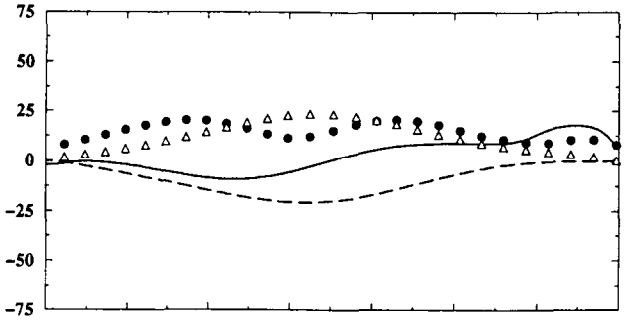


**b)** $x = 50mm$

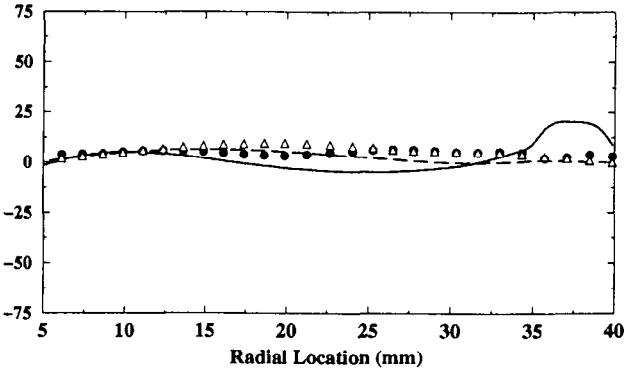


**c)** $x = 35mm$

**Fig. 3 Mean and RMS velocity profiles (m/s) for $U_o$ = 20 m/s (case I) at x = a) 65, b) 50, and c) 35$mm$. $< \widetilde{u} >$ (—), $\widetilde{u}^{RMS}$ (•), $< \widetilde{v} >$ (– –), $\widetilde{v}^{RMS}$ (△).**

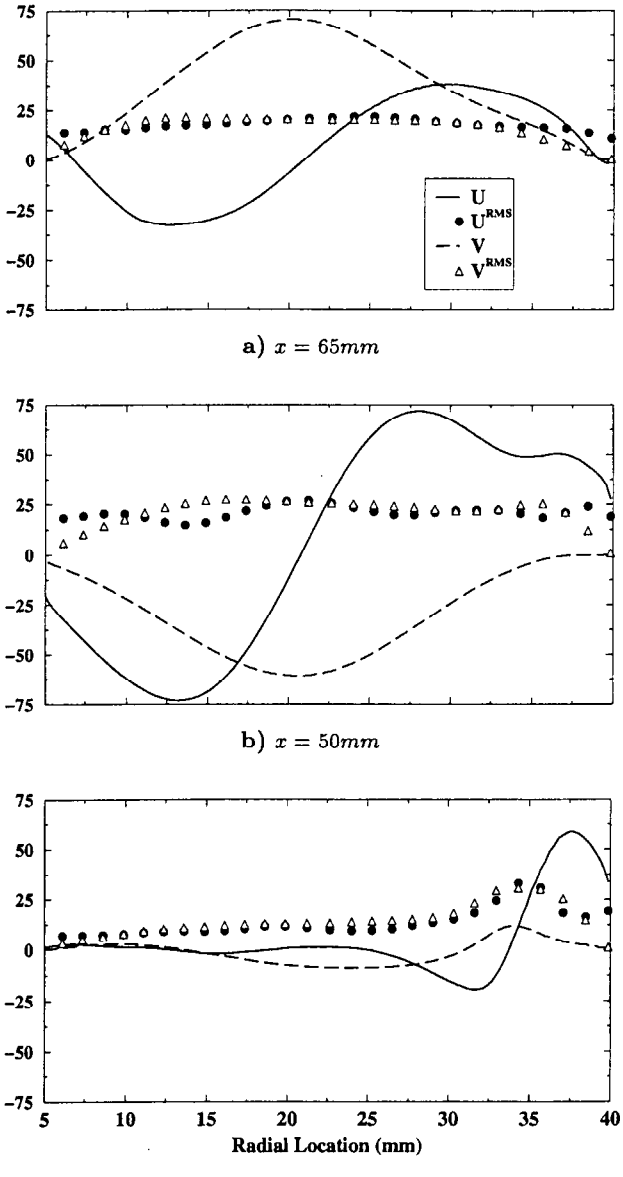


a) $x = 65mm$

b) $x = 50mm$

c) $x = 35mm$

**Fig. 4** Mean and RMS velocity profiles (m/s) for $U_o$ = 40 m/s (case II) at x = a) 65, b) 50, and c) 35$mm$.$< \widetilde{u} >$ (—), $\widetilde{u}^{RMS}$ (•), $< \widetilde{v} >$ (– –), $\widetilde{v}^{RMS}$ (△).

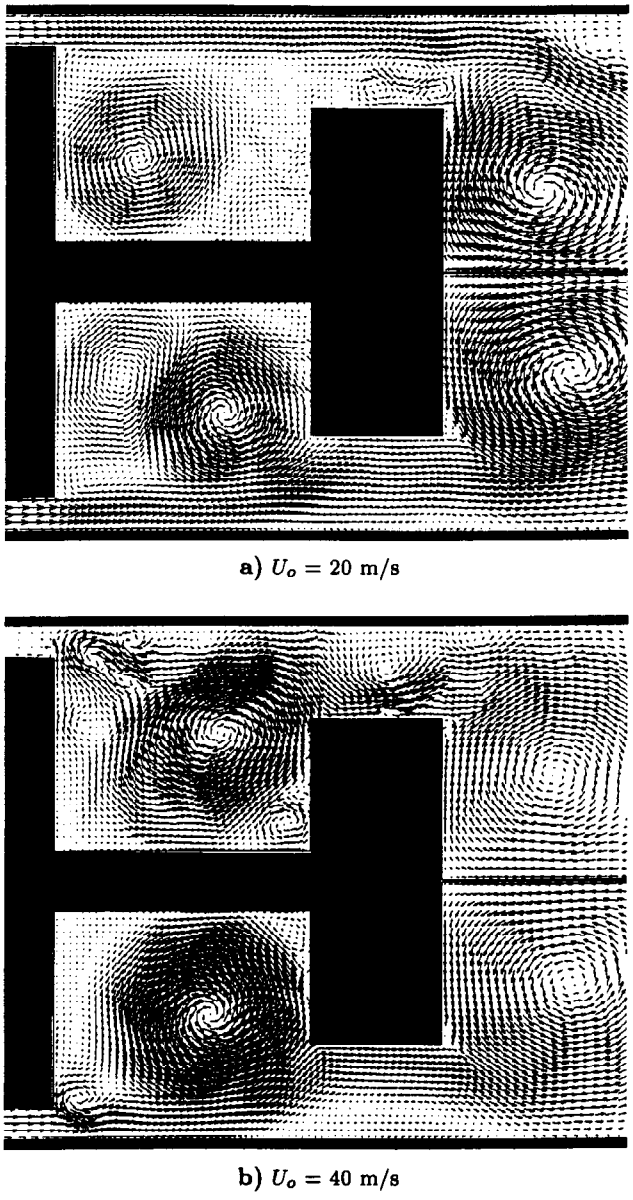

a) $U_o$ = 20 m/s

b) $U_o$ = 40 m/s

**Fig. 5** Non-Reacting velocity vectors for $U_o$ = a) 20 m/s, b) 40 m/s (cases I & II). Upper halves are instantaneous, lower halves are time averaged.

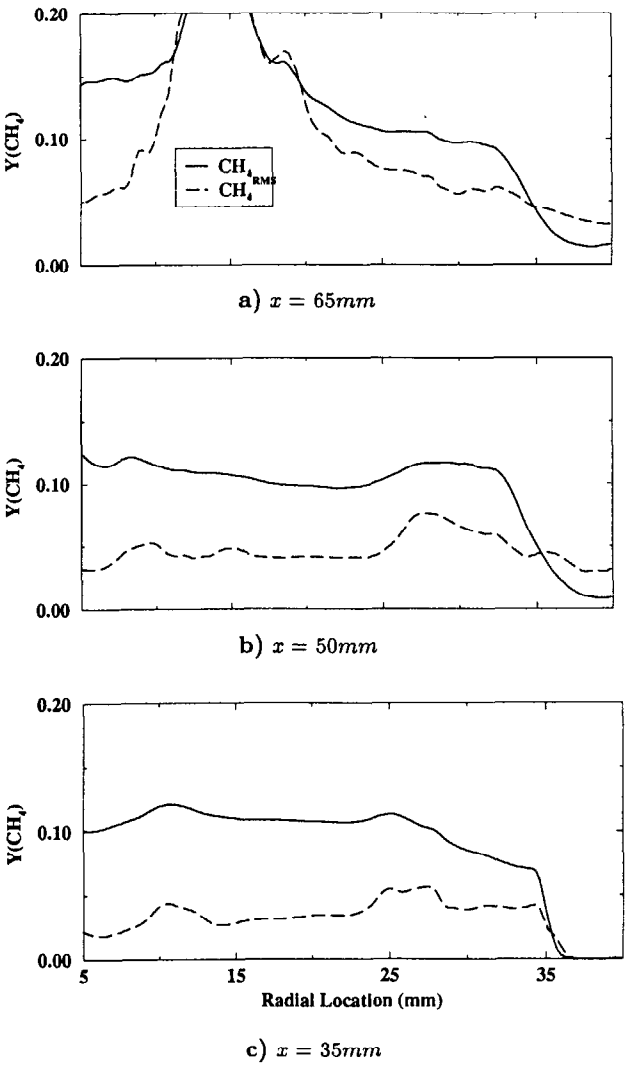


Fig. 6 Mean and RMS fuel mass fraction profiles for $U_o$ = 20 m/s (case I) at x = a) 65, b) 50, and c) 35$mm$. $< \widetilde{Y}_{CH_4} >$ (—), $\widetilde{Y_{CH_4}}^{RMS}$ (– –).

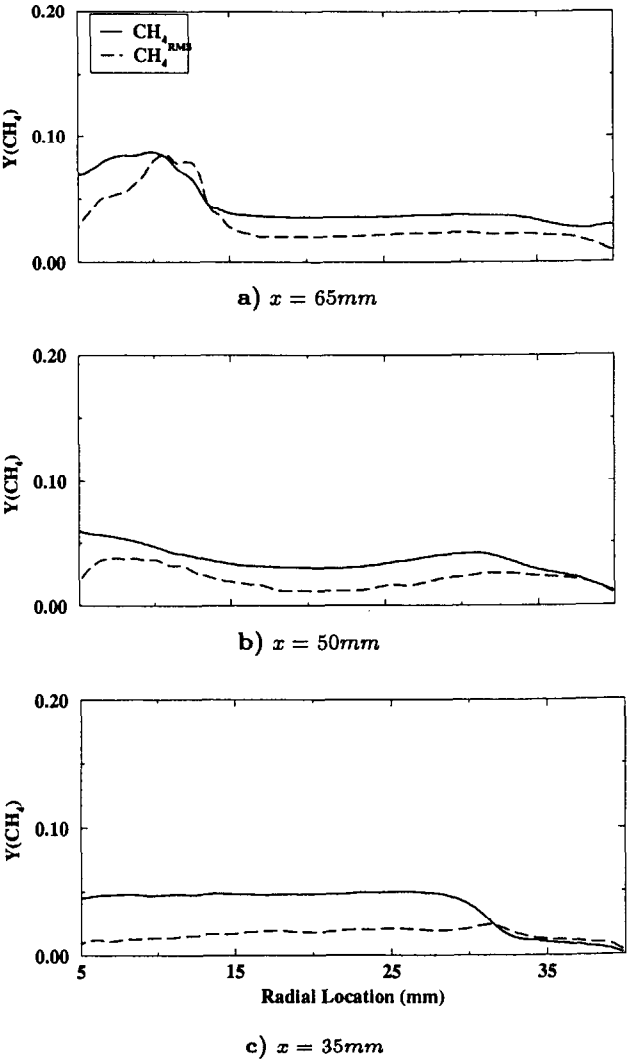


Fig. 7 Mean and RMS fuel mass fraction profiles for $U_o$ = 40 m/s (case II) at x = a) 65, b) 50, and c) 35$mm$. $< \widetilde{Y}_{CH_4} >$ (—), $\widetilde{Y_{CH_4}}^{RMS}$ (– –).

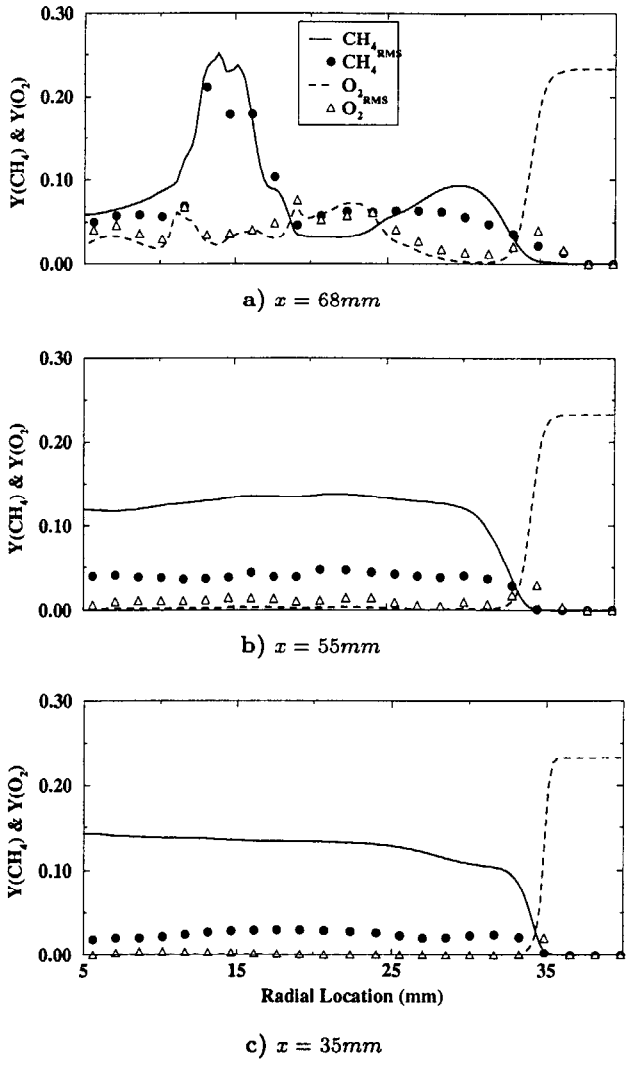


Fig. 8 Mean and RMS mass fraction profiles for $U_o$ = 20 m/s (case IV) at x = a) 68, b) 55, and c) 35$mm$. $< \widetilde{Y}_{CH_4} >$ (—), $< \widetilde{Y}_{O_2} >$ (– –), $\widetilde{Y}_{CH_4}^{RMS}$ (•), $\widetilde{Y}_{O_2}^{RMS}$ (△).

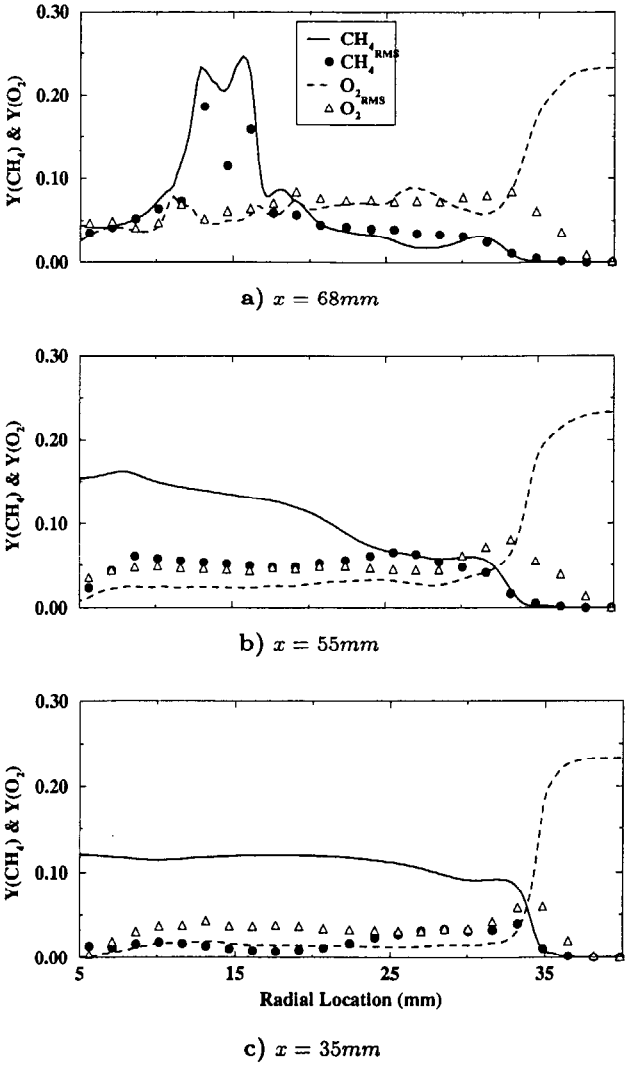


Fig. 9 Mean and RMS mass fraction profiles for $U_o$ = 40 m/s (case V) at x = a) 68, b) 55, and c) 35$mm$. $< \widetilde{Y}_{CH_4} >$ (—), $< \widetilde{Y}_{O_2} >$ (– –), $\widetilde{Y}_{CH_4}^{RMS}$ (•), $\widetilde{Y}_{O_2}^{RMS}$ (△).

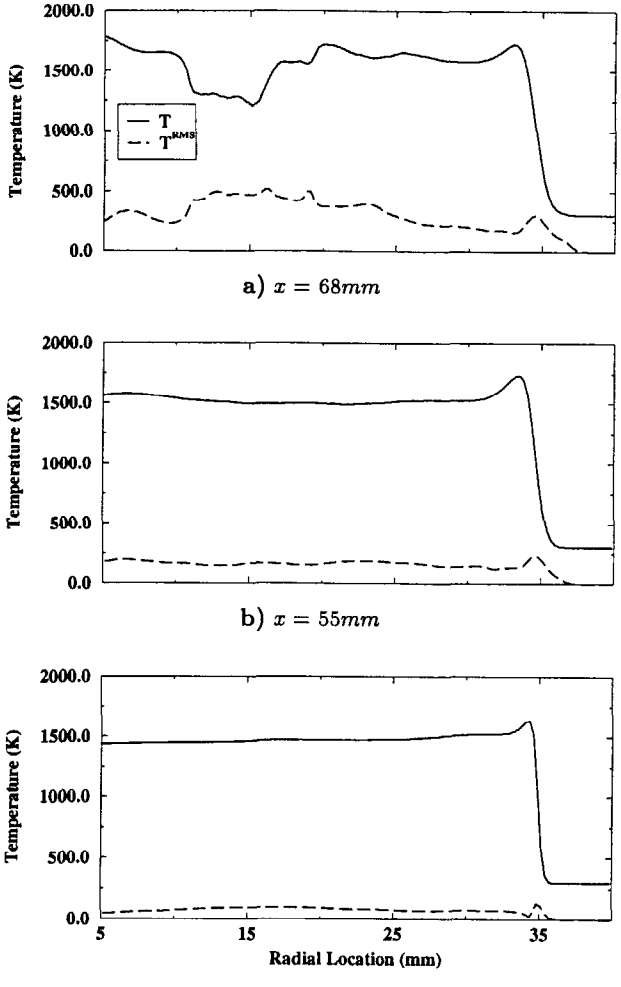


a) $x = 68mm$

b) $x = 55mm$

c) $x = 35mm$

**Fig. 10** Mean and RMS temperature profiles at $x$ = a) 68, b) 55, c) $35mm$ for $U_o$ = 20 m/s (Case IV). $< \widetilde{T} >$ (—), $\widetilde{T}^{RMS}$ (– –).

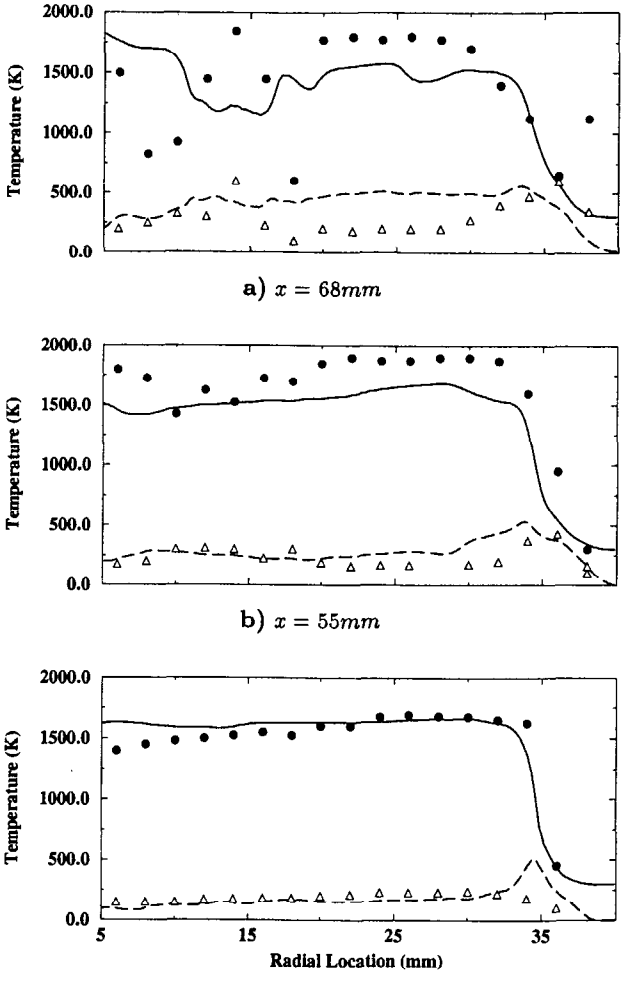


a) $x = 68mm$

b) $x = 55mm$

c) $x = 35mm$

**Fig. 11** Mean and RMS temperature profiles at $x$ = a) 68, b) 55, c) $35mm$ for $U_o$ = 40 m/s (Case V). $< \widetilde{T} >$ (—), $\widetilde{T}^{RMS}$ (– –), $T_{exp}$ (•), $T_{exp}^{RMS}$ (△). Experimental results ($_{exp}$) from Hsu *et al.*[1]

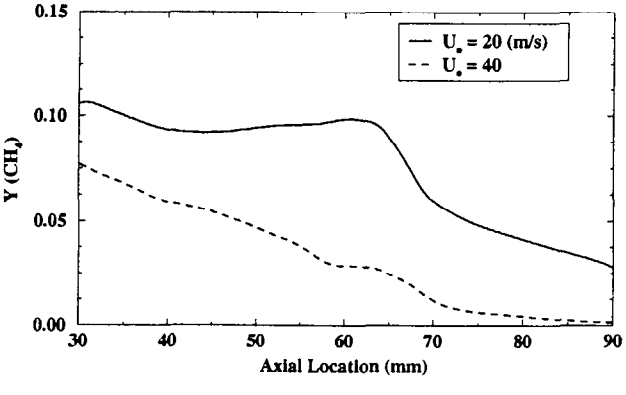


**Fig. 12** Fuel mass fraction ensemble average over dump shear layer region, $25.4mm$ < r < $35mm$, $30mm$ < x < $90mm$.

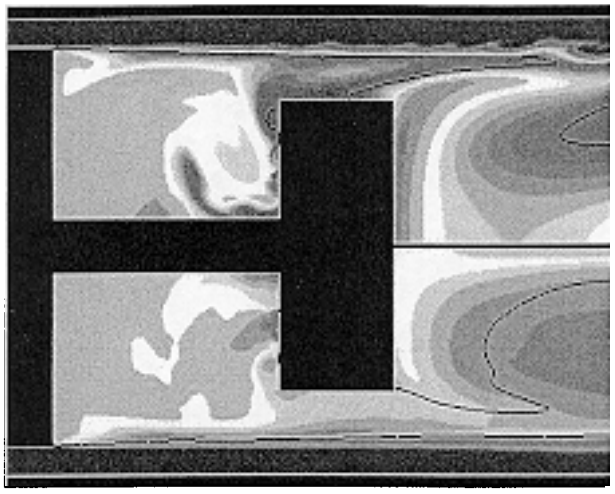

a) $U_o = 20$ m/s

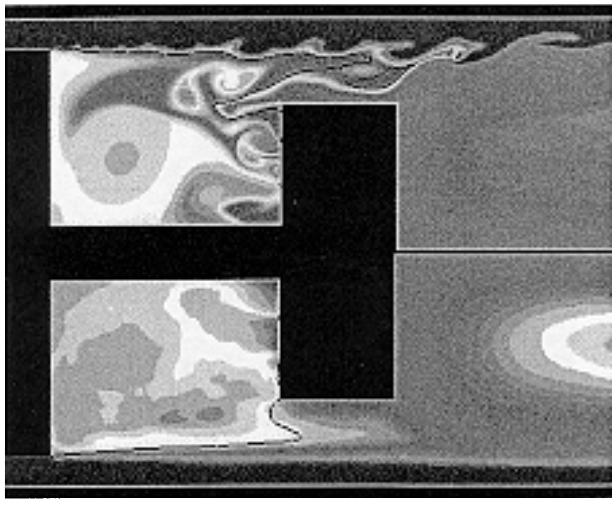

b) $U_o = 40$ m/s

**Fig. 13** Reacting flow temperature field and stoichiometric surface for $U_o$ = a) 20 m/s, b) 40 m/s. Upper halves are instantaneous, lower halves are time averaged. Temperature color contour ranges are 300 K (blue) and 2000 K (red). Stoichiometric mixture fraction, $Z = Z_{st} \simeq 0.055$, shown with black line.

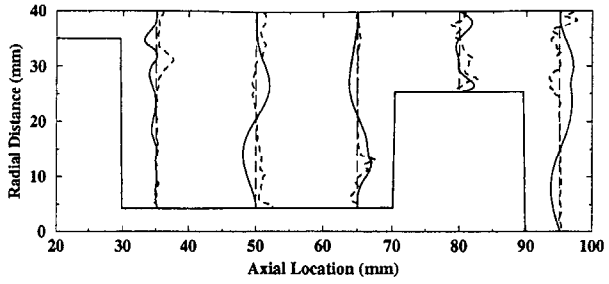


**Fig. 14** Direct calculation of turbulent species transport closure, $-\widetilde{<v''Y''>}$ (dashed–line), vs. fuel mass fraction radial gradient, $\partial \widetilde{<Y>}/\partial y$ (solid), from time averaged LES data. For qualitative analysis, each data profile has been normalized by its maximum value along the radial direction.

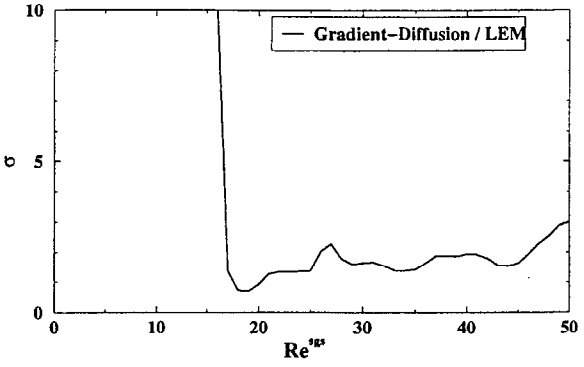


**Fig. 15** Gradient–Diffusion / LEM closure ratio, $\sigma$, as function of $\mathrm{Re}^{sgs}$ (—).

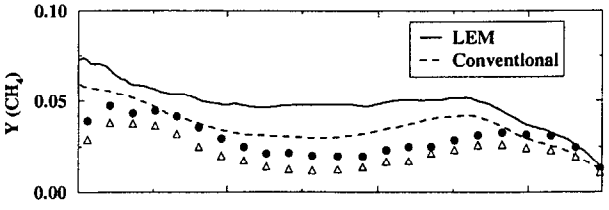


a) $x = 50mm$

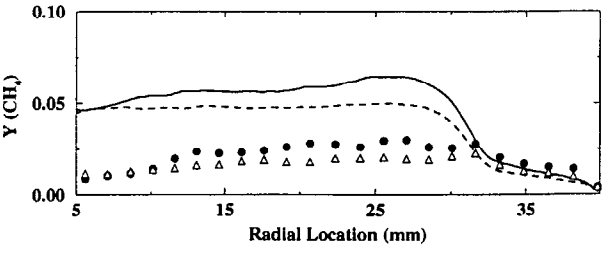


b) $x = 35mm$

**Fig. 16** Fuel mass fraction radial profiles at $x$ = a) 50 and b) $35mm$. $< \widetilde{Y}_{CH_4} >_{LEM}$ (—), $< \widetilde{Y}_{CH_4} >_{Grad-Diff}$ (– –), $\widetilde{Y}^{RMS}_{LEM}$ (•), $\widetilde{Y}^{RMS}_{Grad-Diff}$ (△).